

WGFormer: An SE(3)-Transformer Driven by Wasserstein Gradient Flows for Molecular Ground-State Conformation Prediction

Fanmeng Wang¹ Minjie Cheng¹ Hongteng Xu^{1,2*}

¹Gaoling School of Artificial Intelligence, Renmin University of China

²Beijing Key Laboratory of Big Data Management and Analysis Methods

Abstract

Predicting molecular ground-state conformation (i.e., energy-minimized conformation) is crucial for many chemical applications such as molecular docking and property prediction. Classic energy-based simulation is time-consuming when solving this problem while existing learning-based methods have advantages in computational efficiency but sacrifice accuracy and interpretability. In this work, we propose a novel and effective method to bridge the energy-based simulation and the learning-based strategy, which designs and learns a Wasserstein gradient flow-driven SE(3)-Transformer, called WGFormer, for molecular ground-state conformation prediction. Specifically, our method tackles this task within an auto-encoding framework, which encodes low-quality conformations by the proposed WGFormer and decodes corresponding ground-state conformations by an MLP. The architecture of WGFormer corresponds to Wasserstein gradient flows — it optimizes molecular conformations by minimizing an energy function defined on the latent mixture models of atoms, thereby significantly improving performance and interpretability. Extensive experiments show that our method consistently outperforms state-of-the-art competitors, providing a new and insightful paradigm to predict molecular ground-state conformation. The code is available at <https://github.com/FanmengWang/WGFormer>.

1 Introduction

Molecular ground-state conformation represents the most stable 3D molecular structure corresponding to the energy-minimized state on the potential energy surface. It determines many important molecular properties [1] and thus plays a crucial role in various downstream applications like molecular docking [2, 3] and property prediction [4, 5]. Traditionally, molecular ground-state conformation can be obtained through various energy-based simulation methods, e.g., molecular dynamics (MD) simulation [6] and density functional theory (DFT) calculation [7, 8]. However, these methods are too expensive and computationally slow to meet the growing enormous demands [9]. Although some cheminformatic tools like RDKit [10] have been developed to generate molecular conformations efficiently, they suffer undesired precision in obtaining molecular ground-state conformation.

Recently, with the significant advancement of artificial intelligence in the scientific field [11, 12], learning-based methods have emerged as a promising solution to tackle this task [1]. Early methods like ConfVAE [13] employ various generative models to generate multiple potential low-energy conformations and then screen energy-minimized conformation among them, which lack the guarantee of obtaining ground-state conformation due to the uncertainty of the two-stage process [1]. In this context, subsequent efforts have shifted to design specialized methods to predict molecular ground-state conformation directly [14]. Among them, some state-of-the-art methods, e.g., ConfOpt [15], formulate ground-state conformation prediction as an optimization problem, which takes low-quality 3D conformations as input and optimizes the conformations accordingly. Essentially, these methods apply neural networks to predict the gradient field of the conformational energy landscape and thus imitate gradient descent to update the input conformations. However, their

*Corresponding author: Hongteng Xu (hongtengxu@ruc.edu.cn)

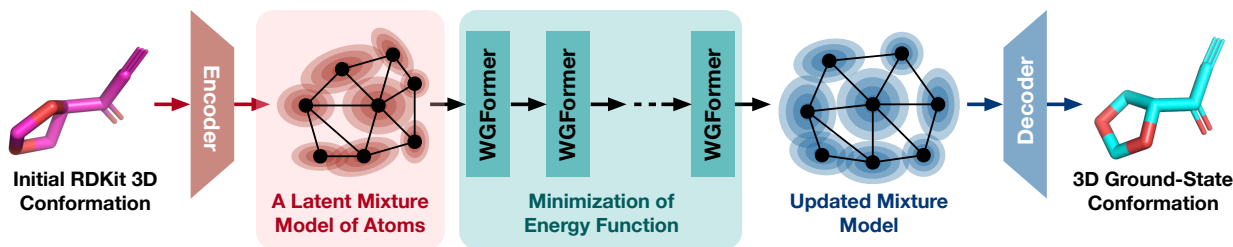


Figure 1: The illustration of the proposed model architecture, in which our WGFormer corresponds to Wasserstein gradient flows and minimizes a physically reasonable energy function defined on the latent mixture model of atoms.

neural networks are designed empirically, making the feedforward computations generally not correspond to minimizing a physically meaningful energy function of conformations. Therefore, such empirical neural network architectures not only harm the model interpretability but also lead to sub-optimal performance.

In this work, considering that low-quality conformation can be readily available [16, 17], and specialized model architectures designed for 3D molecules have made great progress [18, 19], we design and learn a Wasserstein gradient flow-driven SE(3)-Transformer, called WGFormer, to obtain molecular ground-state conformation through optimizing the corresponding low-quality conformation. As illustrated in Figure 1, our method tackles this task within an auto-encoding framework, where we first encode low-quality conformations (e.g., those generated by RDKit) through our WGFormer, and then decode the corresponding ground-state conformations through a simple multi-layer perceptron (MLP). Inspired by the Sinkformer in [20], WGFormer adjusts query, key, and value matrices and applies the Sinkhorn-scaling algorithm [21] to compute attention maps that involve relational information. Such an architecture makes our WGFormer work as Wasserstein gradient flows [22] under specific conditions, which minimizes an energy function defined on the latent mixture models of atoms, significantly improving the model performance and interpretability.

To the best of our knowledge, our method makes the first attempt to predict molecular ground-state conformation through the lens of Wasserstein gradient flows, which leads to a new and interpretable model architecture for molecular modeling. Extensive experiments demonstrate that our method significantly outperforms state-of-the-art methods across different datasets, achieving promising molecular ground-state conformation prediction results. Meanwhile, comprehensive ablation studies further offer valuable insights into our method, including the rationality of the WGFormer architecture, its robustness to data noise, and its computational efficiency advantage.

2 Related Work

2.1 Molecular Conformation Generation

In recent years, many molecular conformation generation methods have been developed. Early methods like CVGAE [23] apply variational autoencoders [24] to generate conformations. CGCF [25] and ConfGF [26] are further proposed to enhance the performance through normalizing flows [27] and score-based generative models [28], respectively. Recently, some methods like GeoDiff [29] and TorDiff [30] leverage popular diffusion models [31] to generate conformations. However, these methods are designed to generate “reasonable” rather than ground-state conformations.

Focusing on molecular ground-state conformation prediction, the work in [14] first proposes the Molecule3D benchmark with ground-state conformations and develops a graph neural network-based solution. GTMGC [1] formally defines this task and predicts molecular ground-state conformation based on Graph Transformer [32]. REBIND [33] improves GTMGC by adding edges to molecular graphs based on the Lennard-Jones potential, which captures non-bonded interactions for low-degree atoms. However, these methods predict ground-state conformations merely based on 2D molecular graphs, whose input information is insufficient to generate high-quality conformations.

Recently, some methods like ConfOpt [15] formulate ground-state conformation prediction from the perspective of conformation optimization. They take low-quality 3D conformations as input and apply various Transformer models to predict the gradient field of the conformational energy landscape [34]. Accordingly, the feedforward steps of their models correspond to optimizing the input conformation by gradient descent. However, the empirical architectures of the models prevent them from minimizing a physically meaningful energy function, resulting in limited model interpretability and sub-optimal performance. Although some modified Transformer models have been proposed from the perspective of differential equations [35, 36, 20], they are seldom applied to model structured data like molecular conformations and often ignore the requirement in SE(3)-equivariance.

2.2 Applications of Ground-State Conformation

Since molecular ground-state conformation represents the energy-minimized state on the potential energy surface, where the inter-atomic forces are balanced at equilibrium [33], it plays a crucial role in various downstream applications. For example, considering many physical, chemical, and biological properties of a molecule are determined by its ground-state conformation, these conformations are extensively utilized in molecular property prediction [4, 5] and molecular docking [2, 3]. Furthermore, while 3D molecular pretraining has greatly enhanced the performance of various molecule-related tasks [16, 37], it has also dramatically increased the demand for high-quality 3D molecular structure data, underscoring the critical need to develop efficient and accurate methods for obtaining molecular ground-state conformations.

3 Proposed Model

3.1 An Auto-Encoding Framework for Ground-State Conformation Prediction

We denote the molecular graph with N atoms as $\mathcal{G} = (\mathcal{V}, \mathcal{E})$, where $\mathcal{V} = \{v_i\}_{i=1}^N$ is the set of atoms and $\mathcal{E} = \{e_{ij}\}_{i,j=1}^N$ is the set of edges representing interatomic bonds. For the corresponding ground-state conformation, each atom is embedded by a 3D coordinate vector $\mathbf{c} \in \mathbb{R}^3$ and the ground-state conformation can be represented as $\mathbf{C} = [\mathbf{c}_i] \in \mathbb{R}^{N \times 3}$. In addition, the interatomic distances are further denoted as $\mathbf{D} = [d_{ij}] \in \mathbb{R}^{N \times N}$, where $d_{ij} = \|\mathbf{c}_i - \mathbf{c}_j\|_2$ is the Euclidean distance between the i -th and j -th atom.

Following previous work [1], we apply RDKit ETKDG [38] to obtain initial low-quality conformation for the molecular graph \mathcal{G} , denoted as $\tilde{\mathbf{C}} = [\tilde{\mathbf{c}}_i] \in \mathbb{R}^{N \times 3}$. Given the graph structure \mathcal{G} and the initial conformation $\tilde{\mathbf{C}}$, we aim to design and learn a model to predict the ground-state conformation, i.e., $\hat{\mathbf{C}} = g_\theta(\mathcal{G}, \tilde{\mathbf{C}})$, where $\hat{\mathbf{C}} = [\hat{\mathbf{c}}_i] \in \mathbb{R}^{N \times 3}$ contains the atom coordinates of predicted ground-state conformation and g_θ is the target model with learnable parameter θ . In this study, we tackle this task from the perspective of conformation optimization, designing g_θ in an auto-encoding framework.

Encoder. We first extract the initial atom-level representation $\mathbf{X}^{(0)} = [\mathbf{x}_i^{(0)}] \in \mathbb{R}^{N \times D}$ and interatomic relational representation $\mathbf{R}^{(0)} = [\mathbf{r}_{ij}^{(0)}] \in \mathbb{R}^{N \times N \times H}$ from \mathcal{G} and $\tilde{\mathbf{C}}$, respectively. For $i, j = 1, \dots, N$, we have

$$\mathbf{x}_i^{(0)} = f(v_i), \quad \mathbf{r}_{ij}^{(0)} = \mathcal{N}(\tilde{d}_{ij} \mathbf{u}_{v_i v_j} + \mathbf{v}_{v_i v_j}; \boldsymbol{\mu}, \boldsymbol{\sigma}), \quad (1)$$

where f embeds each atom type to a D -dimensional vector $\mathbf{x}_i^{(0)}$, $\tilde{d}_{ij} = \|\tilde{\mathbf{c}}_i - \tilde{\mathbf{c}}_j\|_2$ is the interatomic distance, $\mathcal{N}(\cdot; \boldsymbol{\mu}, \boldsymbol{\sigma})$ is a Gaussian kernel function [39] with learnable mean value $\boldsymbol{\mu} \in \mathbb{R}^H$ and standard deviation $\boldsymbol{\sigma} \in \mathbb{R}^H$, $\mathbf{u}_{v_i v_j} \in \mathbb{R}^H$ and $\mathbf{v}_{v_i v_j} \in \mathbb{R}^H$ represent the learnable weight and bias for each atom type pair (v_i, v_j) . Note that, we ensure that $\mathbf{u}_{v_i v_j} = \mathbf{u}_{v_j v_i}$ and $\mathbf{v}_{v_i v_j} = \mathbf{v}_{v_j v_i}$, leading to symmetric relational representation.

Then, we derive the final atom-level and relational representations by passing the initial $\{\mathbf{X}^{(0)}, \mathbf{R}^{(0)}\}$ through L proposed WGFormer layers, i.e.,

$$\mathbf{X}^{(L)}, \mathbf{R}^{(L)} = \text{WGFormer}_L(\mathbf{X}^{(0)}, \mathbf{R}^{(0)}), \quad (2)$$

where WGFormer_L refers to the architecture formed by stacking L WGFormer layers together.

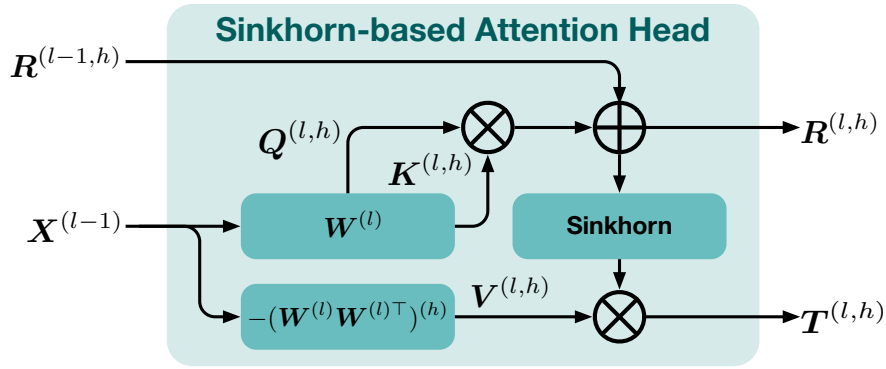


Figure 2: An illustration of the h -th head in the l -th WGFormer.

Decoder. Given the initial and final representations, we design an MLP-based decoder to obtain the predicted ground-state conformation $\hat{\mathbf{C}}$. For $i = 1, \dots, N$, we have

$$\hat{\mathbf{c}}_i = \tilde{\mathbf{c}}_i + \sum_{j=1}^N \frac{\text{MLP}(\mathbf{r}_{ij}^{(L)} - \mathbf{r}_{ij}^{(0)})(\tilde{\mathbf{c}}_i - \tilde{\mathbf{c}}_j)}{N}, \quad (3)$$

where $\hat{\mathbf{c}}_i \in \mathbb{R}^3$ is the predicted 3D coordinate of the i -th atom in the ground-state conformation and $\tilde{\mathbf{c}}_i \in \mathbb{R}^3$ is the initial 3D coordinate of the i -th atom. The proposed decoder predicts the residual between $\hat{\mathbf{c}}_i$ and $\tilde{\mathbf{c}}_i$ by the weighted average of the displacement vectors from $\tilde{\mathbf{c}}_i$ to the other coordinates (i.e., $\{\tilde{\mathbf{c}}_i - \tilde{\mathbf{c}}_j\}_{j=1}^N$). The weights of the displacement vectors are determined by the MLP, which takes the residual between $\mathbf{r}_{ij}^{(L)}$ and $\mathbf{r}_{ij}^{(0)}$ as input. In addition, combined with Eq. 1, we can easily prove that our whole auto-encoding framework is SE(3)-equivariant (Appendix A).

The proposed WGFormer plays a central role in our model. In the following content, we will introduce its architecture in detail and further interpret it from the perspective of Wasserstein gradient flows.

3.2 The Architecture of WGFormer

Inspired by the Sinkformer in [20], the proposed WGFormer implements attention maps based on the Sinkhorn-scaling algorithm [21]. Consider the WGFormer in the l -th layer, which takes $\{\mathbf{X}^{(l-1)}, \mathbf{R}^{(l-1)}\}$ as input and obtains $\{\mathbf{X}^{(l)}, \mathbf{R}^{(l)}\}$ accordingly. It contains H attention heads, each of which corresponds to a channel of the tensor $\mathbf{R}^{(l-1)}$, i.e., $\mathbf{R}^{(l-1,h)} \in \mathbb{R}^{N \times N}$ for $h = 1, \dots, H$. As illustrated in Figure 2, the attention head is implemented by the following five steps:

- 1) $\mathbf{Q}^{(l,h)} = \mathbf{K}^{(l,h)} = \mathbf{X}^{(l-1)} \mathbf{W}^{(l,h)}$,
- 2) $\mathbf{A}^{(l,h)} = (\mathbf{W}^{(l)} \mathbf{W}^{(l)\top})^{(h)}$,
- 3) $\mathbf{V}^{(l,h)} = -\mathbf{X}^{(l-1)} \mathbf{A}^{(l,h)}$,
- 4) $\mathbf{R}^{(l,h)} = \mathbf{R}^{(l-1,h)} + \frac{\mathbf{Q}^{(l,h)} (\mathbf{K}^{(l,h)})^\top}{\sqrt{D_a}}$,
- 5) $\mathbf{T}^{(l,h)} = \kappa^M(\mathbf{R}^{(l,h)}) \mathbf{V}^{(l,h)}$,

where $\mathbf{W}^{(l)} = [\mathbf{W}^{(l,1)}, \dots, \mathbf{W}^{(l,H)}] \in \mathbb{R}^{D \times D}$ is a learnable matrix and the submatrix $\mathbf{W}^{(l,h)} \in \mathbb{R}^{D \times D_a}$ corresponds to the h -th attention head, with $D_a = D/H$. $(\mathbf{W}^{(l)} \mathbf{W}^{(l)\top})^{(h)} \in \mathbb{R}^{D \times D_a}$ means that we first compute $\mathbf{W}^{(l)} \mathbf{W}^{(l)\top}$, denoted as $\mathbf{A}^{(l)} = [\mathbf{A}^{(l,1)}, \dots, \mathbf{A}^{(l,H)}]$, where $\mathbf{A}^{(l,h)} \in \mathbb{R}^{D \times D_a}$ for $h = 1, \dots, H$, and then preserving the h -th submatrix $\mathbf{A}^{(l,h)}$; $\kappa^M(\cdot)$ denotes the Sinkhorn-scaling algorithm [21], passing a matrix through an elementwise exponential operation and normalizing its rows and columns alternatively in M

steps, i.e., $\forall \mathbf{R} \in \mathbb{R}^{N \times N}$,

$$\kappa^M(\mathbf{R}) = \underbrace{N_c \circ N_r \circ \dots \circ N_c \circ N_r}_{M \text{ steps}}(\exp(\mathbf{R})), \quad (5)$$

where $N_r(\mathbf{R}) = \mathbf{R} \oslash (\mathbf{R} \mathbf{1}_{N \times N})$ and $N_c(\mathbf{R}) = \mathbf{R} \oslash (\mathbf{1}_{N \times N} \mathbf{R})$ denote row and column normalization operations, and \oslash denotes element-wise division of matrix. Obviously, κ^0 means the exponential function, i.e., $\kappa^0(\mathbf{R}) = \exp(\mathbf{R})$.

Finally, given $\{\mathbf{T}^{(l,h)}, \mathbf{R}^{(l,h)}\}_{h=1}^H$, WGFormer concatenates them and derive $\mathbf{X}^{(l)}$ and $\mathbf{R}^{(l)}$ as

$$\begin{aligned} \mathbf{X}^{(l)} &= \mathbf{X}^{(l-1)} + \text{Concat}(\{\mathbf{T}^{(l,h)}\}_{h=1}^H), \\ \mathbf{R}^{(l)} &= \text{Concat}(\{\mathbf{R}^{(l,h)}\}_{h=1}^H), \end{aligned} \quad (6)$$

where $\text{Concat}(\cdot)$ denotes the concatenation operation. Stacking L WGFormer modules together and passing $\{\mathbf{X}^{(0)}, \mathbf{R}^{(0)}\}$ through them, we derive the final representations $\{\mathbf{X}^{(L)}, \mathbf{R}^{(L)}\}$, as shown in Eq. 2.

Remarks. Note that, although WGFormer is inspired by the Sinkformer in [20], its architecture is different from Sinkformer in the following three points:

1) Adjusting ‘‘QKV’’ matrices in a different manner: In WGFormer, we set $\mathbf{W}_Q = \mathbf{W}_K = \mathbf{W}^{(l,h)}$ for each head like the work in [40, 20] does. However, for the value matrix, we set it as $(\mathbf{W}^{(l)} \mathbf{W}^{(l)\top})^{(h)} = (\sum_{h'=1}^H \mathbf{W}^{(l,h')} \mathbf{W}^{(l,h')\top})^{(h)}$ for the h -th head. Such an architecture integrates the functionality of feature-level fusion into the attention heads, where the value matrix of each head involves the model parameters shared across different heads.

2) Removing FFN module: Classic Transformer [41] and its variants (including Sinkformer [20]) apply FFN modules to achieve cross-head feature fusion. However, thanks to the above adjustment of the ‘‘QKV’’ matrices (i.e., the second and third steps in Eq. 4), WGFormer has fused features across different attention heads. Therefore, the classic FFN module is abandoned by WGFormer, which simplifies the model architecture and reduces the computational cost. Moreover, without the FFN module, we can study the L stacked WGFormers jointly instead of analyzing a single layer.

3) Encoding relational information: Focusing on ground-state conformation prediction, our auto-encoding framework needs to leverage the interatomic relational information and maintain the SE(3)-equivariance property. The fourth and fifth steps in Eq. 4 indicate that the WGFormer considers the encoding of relational matrices and introduces the matrices into the computation of attention maps.

In the following content, we will show that the above modifications make WGFormer suitable for molecular conformation modeling and maintain its interpretability — under some specific settings, WGFormer works as Wasserstein gradient flows defined on a latent mixture model of atoms.

4 Revisiting WGFormer through the Lens of Wasserstein Gradient Flows

4.1 Continuous Counterpart of Attention Head

Let’s consider a WGFormer with a single attention head (i.e., $H = 1$ and the superscripts l and h in Eq. 4 can be omitted), whose parameter matrix is $\mathbf{W} \in \mathbb{R}^{D \times D}$. Given a conformation with N atom-level representations, we introduce a mixture model of the atoms, i.e.,

$$\mu \in \mathcal{M}(\mathbb{R}^D), \text{ and } \mu = \sum_{i=1}^N \mu_i, \quad (7)$$

where $\mathcal{M}(\mathbb{R}^D)$ is the space of the measures defined in \mathbb{R}^D , and $\mu_i \in \mathcal{M}(\mathbb{R}^D)$ is the measure associated with the i -th atom. For an arbitrary measure pair (μ_i, μ_j) , we describe the relation between μ_i and μ_j quantitatively as

$$r_{ij} = \bar{\mathbf{x}}_i^\top \mathbf{W} \mathbf{W}^\top \bar{\mathbf{x}}_j = \bar{\mathbf{x}}_i^\top \mathbf{A} \bar{\mathbf{x}}_j, \quad (8)$$

where $\bar{\mathbf{x}}_i = \int \mathbf{x} d\mu_i(\mathbf{x})$ for $i = 1, \dots, N$. The collection of the relations leads to a symmetric matrix $\mathbf{R} = [r_{ij}]$.

When each μ_i is a Dirac measure, i.e., $\mu_i = \delta_{\mathbf{x}_i}$, we can equivalently represent the relations by a function:

$$r(\mathbf{x}, \mathbf{x}') = \sum_{i,j=1}^N r_{ij} \delta_{\mathbf{x}_i, \mathbf{x}_j}(\mathbf{x}, \mathbf{x}'), \quad \forall \mathbf{x}, \mathbf{x}' \in \mathbb{R}^D. \quad (9)$$

In such a situation, the update of the atom-level representations in Eq. 6 is the ResNet equation [42], i.e., $\mathbf{X} \rightarrow \mathbf{X} + \mathbf{T}$, which works as a discrete Euler scheme of the ordinary differential equation (ODE) [43, 19, 20], i.e.,

$$\frac{d\mathbf{x}_i(t)}{dt} = T_\mu^M(\mathbf{x}_i(t)), \quad \forall i = 1, \dots, N. \quad (10)$$

Here, $\mathbf{x}_i(t)$ denotes the i -th atom's representation at time t . $T_\mu^M(\mathbf{x})$ is an operator for the measure $\mu = \sum_{i=1}^N \mu_i = \sum_{i=1}^N \delta_{\mathbf{x}_i}$, which is defined as

$$T_\mu^M(\mathbf{x}) = - \int_{\mathbb{R}^D} k^M(\mathbf{x}, \mathbf{x}') \mathbf{A} \mathbf{x}' d\mu(\mathbf{x}'), \quad (11)$$

where $k^M(\mathbf{x}, \mathbf{x}')$ is the continuous counterpart of the Sinkhorn module κ^M in Eq. 4, i.e.,

$$\begin{aligned} k^0(\mathbf{x}, \mathbf{x}') &= \exp(\mathbf{x}^\top \mathbf{A} \mathbf{x}' + r(\mathbf{x}, \mathbf{x}')), \\ k^{m+1}(\mathbf{x}, \mathbf{x}') &= \begin{cases} \frac{k^m(\mathbf{x}, \mathbf{x}')}{\int k^m(\mathbf{x}, \mathbf{x}') d\mu(\mathbf{x}')}, & m \text{ is even,} \\ \frac{k^m(\mathbf{x}, \mathbf{x}')}{\int k^m(\mathbf{x}, \mathbf{x}') d\mu(\mathbf{x})}, & m \text{ is odd.} \end{cases} \end{aligned} \quad (12)$$

Obviously, the collection of $\{T_\mu^M(\mathbf{x}_i)\}_{i=1}^n$ is equivalent to the matrix \mathbf{T} derived by Eq. 4.

4.2 Wasserstein Gradient Flows When $M = 0$ or $\rightarrow \infty$

The ODE in 10 can be equivalently written as a continuity equation [44], i.e.,

$$\partial_t \mu + \operatorname{div}(\mu T_\mu^M) = 0, \quad (13)$$

It has been known that T_μ^M can be the Wasserstein gradient of an energy function $E : \mathcal{M}(\mathbb{R}^D) \mapsto \mathbb{R}$ at μ , i.e.,

$$T_\mu^M = -\nabla_W E(\mu) := -\nabla \left(\frac{\delta E}{\delta \mu}(\mu) \right), \quad (14)$$

where $\frac{\delta E}{\delta \mu}(\mu)$ denotes the first variation of E at μ , which is a function satisfying $\frac{dE(\mu + \varepsilon \rho)}{d\varepsilon}|_{\varepsilon=0} = \int \frac{\delta E}{\delta \mu}(\mu) d\rho$ for every perturbation ρ [22]. In this situation, the continuity equation in Eq. 13 captures the evolution of the measure μ that minimizes the energy function E , and each $\mathbf{x}(t)$ follows $\frac{d\mathbf{x}(t)}{dt} = -\nabla_W E(\mu)$ [45].

Based on Proposition 2 in [20], we demonstrate that for $\mu = \sum_{i=1}^N \delta_{\mathbf{x}_i}$, WGFormer corresponds to Wasserstein gradient flows when $M = 0$ or $M \rightarrow \infty$.

Proposition 4.1. *For $\mu = \sum_{i=1}^N \delta_{\mathbf{x}_i}$, the T_μ^M in Eq. 11 is the Wasserstein gradient flow, i.e., $T_\mu^M = -\nabla_W E^M(\mu)$, when $M = 0$ or $M \rightarrow \infty$. The corresponding energy functions are*

$$E^0(\mu) = \frac{1}{2} \int k^0(\mathbf{x}, \mathbf{x}') d\mu(\mathbf{x}) d\mu(\mathbf{x}'), \quad (15)$$

$$\begin{aligned} E^\infty(\mu) &= \frac{1}{2} \min_{\pi \in \Pi_\mu} \int \log k^0(\mathbf{x}, \mathbf{x}') d\pi(\mathbf{x}, \mathbf{x}') - H(\pi) \\ &= \frac{1}{2} \int k^\infty(\mathbf{x}, \mathbf{x}') \log \frac{k^0(\mathbf{x}, \mathbf{x}')}{k^\infty(\mathbf{x}, \mathbf{x}')} d\mu(\mathbf{x}) d\mu(\mathbf{x}'), \end{aligned} \quad (16)$$

where $\Pi_\mu = \{\pi \in \mathcal{M}(\mathbb{R}^D \times \mathbb{R}^D) \mid \int_{\mathbf{x}} d\pi(\mathbf{x}, \mathbf{x}') = \mu(\mathbf{x}'), \int_{\mathbf{x}'} d\pi(\mathbf{x}, \mathbf{x}') = \mu(\mathbf{x})\}$, and $H(\pi) = -\int \log(\pi) d\pi$ is the entropy of π .

Note that, $E^\infty(\mu)$ is an interpretable energy function for conformation optimization. As shown in Eq. 16, it corresponds to an entropic optimal transport problem [21, 46]. Because $\mu = \sum_{i=1}^N \delta_{\mathbf{x}_i}$, we can rewrite $E^\infty(\mu)$ in the following discrete format:

$$E^\infty(\mu) = \min_{\mathbf{P} \in \Pi_1} \underbrace{\langle \mathbf{XAX}^\top + \mathbf{R}, \mathbf{P} \rangle}_{\text{Penalize cost}} + \underbrace{\langle \mathbf{P}, \log \mathbf{P} \rangle}_{\text{Regularize entropy}}, \quad (17)$$

where $\mathbf{P} \in \Pi_1$ means $\mathbf{P}\mathbf{1}_N = \mathbf{P}^\top\mathbf{1}_N = \mathbf{1}_N$, and \mathbf{P} is the coupling controlling the pairwise relations among the atoms in the latent space. In particular, the first term in Eq. 17 penalizes the cost associated with the interatomic distances determined by $(\mathbf{XAX}^\top + \mathbf{R})$. The long distances lead to a high cost so penalizing this term prevents atoms from being too far away from each other in the latent space. On the contrary, the second term in Eq. 17 regularizes the entropy of \mathbf{P} , preventing atoms from being concentrated together. Minimizing the energy consisting of these two terms is reasonable for conformation optimization — the atoms of the ground-state conformation should have reasonable interatomic distances, avoiding high energy while maintaining the molecular structure.

In summary, by stacking L WGFormer layers and setting a large value for the hyperparameter M , our model achieves the Wasserstein gradient flows defined on the measure of atoms. Given the initial measure $\mu^{(0)}$ corresponding to $\mathbf{X}^{(0)}$ and the initial relational information $\mathbf{R}^{(0)}$, each layer updates the measure, i.e., $\mu^{(l+1)} = \arg \min_{\mu} E^\infty(\mu) + W_2(\mu, \mu^{(l+1)})$, where $W_2(\cdot, \cdot)$ denotes the 2-order Wasserstein distance, and update the relational information $\mathbf{R} = [r_{ij}]$ based on the new measure (by Eq. 8).

When each μ_i is a non-Dirac measure, our WGFormer can still achieve Wasserstein gradient flows when $M = 0$. For each non-Dirac μ_i , we can define an operator as

$$T_{\mu_i}^0(\mathbf{x}) = - \sum_{j=1}^N \int \exp(\mathbf{x}^\top \mathbf{A}\mathbf{x}' + r_{ij}) \mathbf{A}\mathbf{x}' d\mu_j(\mathbf{x}'). \quad (18)$$

Then, we have the following theorem:

Proposition 4.2. *Let $E : \mathcal{M}(\mathbb{R}^D)^N \mapsto \mathbb{R}$ be an energy function for $\{\mu_i\}_{i=1}^N$, which is defined as*

$$E = \frac{1}{2} \sum_{i,j=1}^N \int \exp(\mathbf{x}^\top \mathbf{A}\mathbf{x}' + r_{ij}) d\mu_i(\mathbf{x}) d\mu_j(\mathbf{x}'). \quad (19)$$

For $i = 1, \dots, N$, $T_{\mu_i}^0$ is the Wasserstein gradient flow that $\min_{\mu_i} E$, i.e., $T_{\mu_i}^0 = -\nabla_W E(\mu_i; \{\mu_j\}_{j \neq i})$.

However, for non-Dirac μ_i 's, WGFormer does not correspond to Wasserstein gradient flows in general when $M \rightarrow \infty$ because in this case the relational information r_{ij} in 8 cannot be rewritten as the function in 9. The proofs of the above propositions are shown in Appendix B.

5 Learning Algorithm

Given the predicted molecular ground-state conformation $\widehat{\mathbf{C}}$, we can further derive the predicted interatomic distances $\widehat{\mathbf{D}}$. However, existing learning methods [15, 1, 33] merely consider penalizing the mean-absolute-error (MAE) between $\widehat{\mathbf{D}}$ and the ground truth \mathbf{D} , which may not provide sufficient supervision and thus limits the model performance.

In this study, we design a multi-task learning strategy to train the proposed model, making the model fit the ground-state conformation \mathbf{C} and the corresponding interatomic distances \mathbf{D} jointly.

In particular, given $\widehat{\mathbf{C}}$ and \mathbf{C} , we firstly align \mathbf{C} to $\widehat{\mathbf{C}}$ in the 3D space i.e.,

$$\begin{aligned} \mathbf{C}_0 &= \mathbf{C} - \frac{1}{N} \sum_{i=1}^N \mathbf{c}_i, & \widehat{\mathbf{C}}_0 &= \widehat{\mathbf{C}} - \frac{1}{N} \sum_{i=1}^N \widehat{\mathbf{c}}_i, \\ \mathbf{C}^* &= \mathbf{C}_0 \text{Rot}(\mathbf{C}_0, \widehat{\mathbf{C}}_0) = \mathbf{C}_0 \mathbf{V} \mathbf{U}^\top, \end{aligned} \quad (20)$$

where \mathbf{C}_0 and $\widehat{\mathbf{C}}_0$ are zero-mean atomic 3D coordinates, and \mathbf{C}^* is the aligned ground truth. $\text{Rot}(\mathbf{C}_0, \widehat{\mathbf{C}}_0)$ is the rotation matrix derived by Procrustes analysis [47], in which \mathbf{U} and \mathbf{V} are obtained from the singular value decomposition (SVD) of $\widehat{\mathbf{C}}_0^\top \mathbf{C}_0$.

The final loss function is defined as follows:

$$\mathcal{L} = \mathcal{L}_{\text{main}} + \lambda \mathcal{L}_{\text{aux}} = \underbrace{\frac{1}{N^2} \|\widehat{\mathbf{D}} - \mathbf{D}\|_1}_{\text{MAE}(\widehat{\mathbf{D}}, \mathbf{D})} + \lambda \underbrace{\sqrt{\frac{1}{N} \|\widehat{\mathbf{C}} - \mathbf{C}^*\|_F^2}}_{\text{RMSD}(\widehat{\mathbf{C}}, \mathbf{C}^*)}. \quad (21)$$

where $\text{MAE}(\widehat{\mathbf{D}}, \mathbf{D})$ denotes the mean-absolute-error of $\widehat{\mathbf{D}}$, which is the main loss supervising the predicted interatomic distances $\widehat{\mathbf{D}}$, and $\text{RMSD}(\widehat{\mathbf{C}}, \mathbf{C}^*)$ denotes the root-mean-square-deviation of $\widehat{\mathbf{C}}$, which is the auxiliary loss directly supervising the predicted ground-state conformation $\widehat{\mathbf{C}}$. In addition, $\lambda \geq 0$ is employed to control the significance of the auxiliary loss.

6 Experiments

To demonstrate the effectiveness and efficiency of our method, we compare it with state-of-the-art methods. In addition, we further conduct comprehensive ablation studies to verify the rationality and robustness of our method. Implementation details and experimental results are in this section and Appendix C.

6.1 Experimental Setup

6.1.1 Datasets

Following previous works, we employ the widely used Molecule3D and QM9 datasets to validate the effectiveness of our method. Molecule3D [14] is a large-scale dataset, comprising approximately four million molecules. It provides two dataset-splitting results (i.e., random-splitting and scaffold-splitting) to ensure a comprehensive evaluation. QM9 [48] is a small-scale quantum chemistry dataset, comprising approximately 130,000 molecules with nine heavy atoms. It adopts the identical dataset-splitting strategy described in [49]. Each molecule in these datasets corresponds to a ground-state conformation determined through density functional theory (DFT) calculations.

6.1.2 Baselines

To fully demonstrate the effectiveness of our method, we compare it with state-of-the-art methods in two categories. The first category is the 2D methods predicting ground-state conformations merely based on 2D molecular graphs, including GTMGC [1] and its variants respectively using GINE [50], GATv2 [51], and GPS [52] as backbones. The second category is the 3D methods predicting ground-state conformations via conformation optimization, including ConfOpt [15] (its TwoAtom and ThreeAtom versions) and its variants respectively using SE(3)-Transformer [18] and EGNN [19] as backbones. All the baselines are implemented based on their default settings.

6.1.3 Implementation and Evaluation

Our model comprises 30 WGFormer layers, each equipped with 64 attention heads. The atom-level and relational representation dimensions are set to 512 and 64, respectively. We train each model on a single NVIDIA RTX 3090 GPU to guarantee a fair assessment while each model is the optimal checkpoint on the corresponding validation set. Besides, we follow the experimental setting in [1], applying mean-absolute-error of distances (D-MAE), root-mean-squared-error of distances (D-RMSE), and root-mean-square-deviation of coordinates (C-RMSD) to evaluate each model on both validation and test sets.

Table 1: The performance comparison for various methods

Dataset	Method	Model	Validation			Test		
			D-MAE ↓	D-RMSE ↓	C-RMSD ↓	D-MAE ↓	D-RMSE ↓	C-RMSD ↓
Molecule3D (random)	2D	GINE	0.590	1.014	1.116	0.592	1.018	1.116
		GATv2	0.563	0.983	1.082	0.564	0.986	1.083
		GPS	0.528	0.909	1.036	0.529	0.911	1.038
		GTMGC	0.432	0.719	<u>0.712</u>	0.433	0.721	<u>0.713</u>
	3D	SE(3)-Transformer	0.466	0.712	0.800	0.467	0.774	0.802
		EGNN	0.461	0.704	0.798	0.462	0.766	0.799
		ConfOpt-TwoAtom	0.438	0.668	0.748	0.438	0.670	0.749
		ConfOpt-ThreeAtom	<u>0.429</u>	<u>0.659</u>	0.734	<u>0.430</u>	<u>0.661</u>	0.736
		WGFormer (ours)	0.391	0.649	0.662	0.392	0.652	0.664
Molecule3D (scaffold)	2D	GINE	0.883	1.517	1.407	1.400	2.224	1.960
		GATv2	0.778	1.385	1.254	1.238	2.069	1.752
		GPS	0.538	0.885	1.031	0.657	1.091	1.136
		GTMGC	0.406	0.675	<u>0.678</u>	0.400	0.679	0.693
	3D	SE(3)-Transformer	0.460	0.676	0.775	0.456	0.678	0.747
		EGNN	0.448	0.666	0.758	0.442	0.670	0.741
		ConfOpt-TwoAtom	0.408	0.626	0.708	0.402	0.628	0.698
		ConfOpt-ThreeAtom	<u>0.401</u>	<u>0.619</u>	0.697	<u>0.395</u>	<u>0.622</u>	<u>0.691</u>
		WGFormer (ours)	0.363	0.599	0.618	0.360	0.610	0.627
QM9	2D	GINE	0.357	0.673	0.685	0.357	0.669	0.693
		GATv2	0.339	0.663	0.661	0.339	0.659	0.666
		GPS	0.326	0.644	0.662	0.326	0.640	0.666
		GTMGC	0.262	0.468	0.362	0.264	0.470	0.367
	3D	SE(3)-Transformer	0.254	0.451	0.296	0.256	0.455	0.303
		EGNN	0.248	0.442	0.257	0.251	0.449	0.265
		ConfOpt-TwoAtom	0.245	0.439	0.245	0.248	0.444	0.254
		ConfOpt-ThreeAtom	<u>0.241</u>	<u>0.433</u>	0.237	<u>0.244</u>	0.438	<u>0.246</u>
WGFormer (ours)	0.223	0.416	0.198	0.227	0.422	0.206		

6.2 Comparisons

Table 1 summarizes the performance of various methods, where WGFormer consistently outperforms all baselines across all evaluation metrics on all datasets. Specifically, compared to the best baseline, WGFormer reduces C-RMSD (the most important metric in this task) by nearly 10% on Molecule3D and by 16% on QM9, demonstrating its exceptional capability. WGFormer also consistently dominates both random and scaffold splits of Molecule3D, demonstrating its effectiveness under different data-splitting strategies. In Figure 3, we visualize several ground-state conformations predicted by our method and the top-3 baselines (GTMGC, ConfOpt-TwoAtom, and ConfOpt-ThreeAtom). As shown in this figure, the ground-state conformations predicted by WGFormer align more closely with the ground truth.

Figure 4 compares the efficiency of our model and the top-3 baselines by calculating the average time taken per molecule on each dataset. Even if our model applies 30 WGFormer layers, it is significantly faster than the baselines, reducing the runtime per molecule by over 50%. One important reason for this superior performance is the simplicity of our WGFormer architecture. WGFormer removes the FFN module and updates the atom-level and relational representations simultaneously. On the contrary, each layer of ConfOpt applies two modules to update the atom-level and relational representations sequentially. ConfOpt-ThreeAtom further considers the relations within the triplets of atoms, which significantly increases the model complexity and computational cost. In summary, the above quantitative and qualitative comparisons clearly highlight the superiority of our WGFormer in both accuracy and efficiency for ground-state conformation prediction.

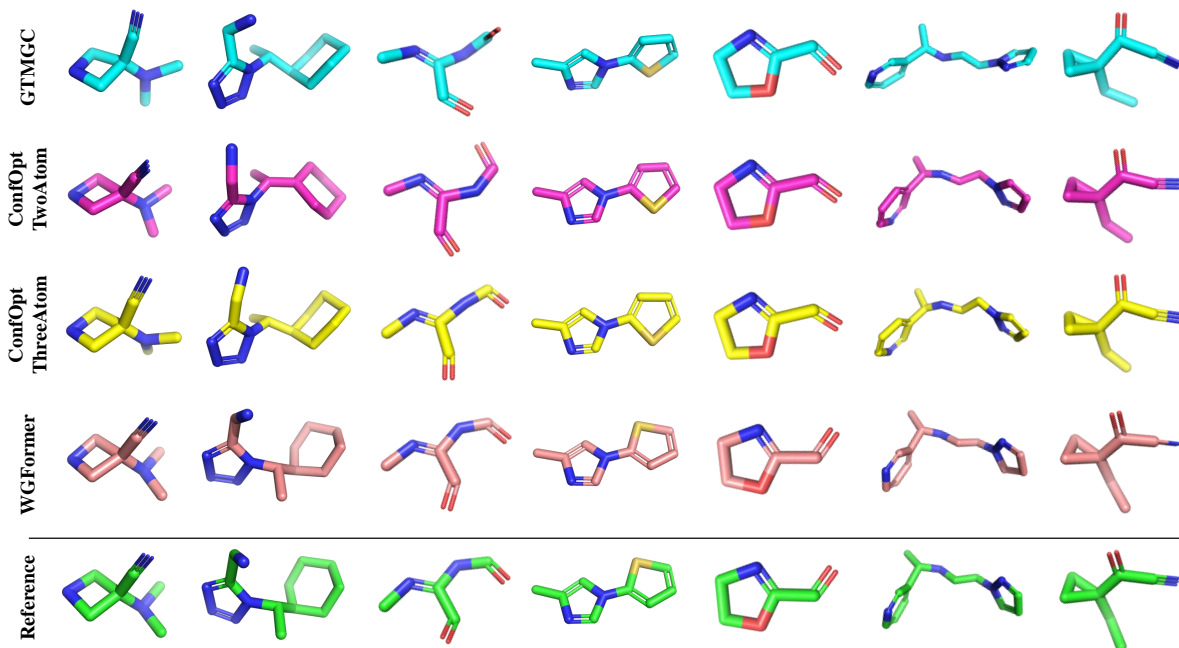


Figure 3: The visual comparison for the ground-state conformations predicted by different methods.

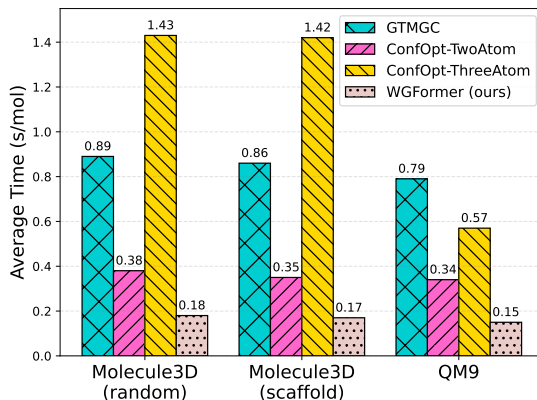


Figure 4: The efficiency comparison between our WGFormer and the top-3 baselines on each dataset.

6.3 Ablation Studies and Robustness Analysis

Rationality of multi-task learning. We conduct an ablation study of our learning strategy on random-split Molecule3D. As shown in Table 2, merely minimizing $\text{RMSD}(\hat{\mathbf{C}}, \mathbf{C}^*)$ performs worse than minimizing $\text{MAE}(\hat{\mathbf{D}}, \mathbf{D})$. This phenomenon aligns with previous works prioritizing optimizing interatomic distances over atomic 3D coordinates, proving the importance of emphasizing optimizing interatomic distances during training. Moreover, compared with merely minimizing a single loss, minimizing them jointly achieves better performance, especially in the key metric C-RMSD, which supports the rationality of our multi-task learning.

Rationality of WGFormer architecture. Besides the theoretical analysis in Section 4, we further demonstrate the rationality of our model architecture through experiments. Here, we conduct an ablation study for the proposed Sinkhorn-based attention head on scaffold-split Molecule3D. In particular, different from the classic attention module, WGFormer applies the Sinkhorn-based attention with the proposed ‘‘QKV’’ adjustment. The results in Table 3 show that *i*) each single modification does not harm the model performance, and *ii*) applying the two modifications jointly leads to significant performance improvements, especially in the most critical metric C-RMSD. These empirical findings align closely with our theoretical analysis in Section 4, further validating the rationality behind the proposed architecture design.

Table 2: The ablation study of multi-task learning strategy.

	\mathcal{L}_{MAE}	$\mathcal{L}_{\text{RMSD}}$	D-MAE ↓	D-RMSE ↓	* C-RMSD ↓
Validation	×	✓	0.652	0.921	0.716
	✓	×	0.384	0.657	0.688
	✓	✓	0.391	0.649	0.662
Test	×	✓	0.653	0.924	0.718
	✓	×	0.386	0.660	0.689
	✓	✓	0.392	0.652	0.664

* refers to the indicator we mainly focus on.

Table 3: The ablation study of our attention head.

	Sinkhorn Module	QKV Adjustment	D-MAE ↓	D-RMSE ↓	C-RMSD ↓
Validation	×	×	0.379	0.628	0.661
	✓	×	0.378	0.631	0.656
	×	✓	0.379	0.625	0.658
	✓	✓	0.363	0.599	0.618
Test	×	×	0.375	0.636	0.662
	✓	×	0.376	0.644	0.662
	×	✓	0.376	0.635	0.665
	✓	✓	0.360	0.610	0.627

Impact of layer numbers on conformation optimization. Our model corresponds to minimizing an energy function, and each layer works as an update step in the Euler scheme of ODE. Without the loss of generality, we assume that the optimization starts at $t = 0$ and ends at $t = 1$. Learning our model with L WGFormer layers results in applying L optimization steps in the time interval $[0, 1]$, and accordingly, the step size is $\Delta t = \frac{1}{L}$.

We quantitatively analyze the impact of layer numbers and thus further verify the optimization nature of our model. In particular, we train two models with 10 and 30 WGFormer layers, respectively. Given each trained model, we evaluate its performance using different layer numbers on QM9, so that we can observe the optimization process achieved by each model and analyze the convergence rate and optimization efficiency. As illustrated in Figure 5, the performance of our models improves steadily as the number of their WGFormer layers increases. The 30-layer WGFormer model performs better, which matches the common sense of optimization: Learning a large number of layers means applying fine-grained optimization with more steps, which leads to lower energy and improved model performance while increasing runtime. These results demonstrate that our model indeed achieves conformation optimization.

Robustness to data noise. In the inference phase, we add Gaussian noise to the coordinates of input conformations and then evaluate our model performance on QM9. As shown in Figure 6, our model achieves stable performance across various noise levels, demonstrating its robustness to data noise. The robustness of our model ensures reliable ground-state conformation prediction even in the presence of perturbations.

7 Conclusion

In this work, we propose WGFormer, a Wasserstein gradient flow-driven SE(3)-Transformer that effectively tackles the molecular ground-state conformation prediction task. Specifically, WGFormer can be interpreted as Wasserstein gradient flows, which optimizes molecular conformation by minimizing a physically reasonable energy function. In the future, we will continue to explore the applications of our method in various conformation-related tasks. In addition, we will further study the mathematics of WGFormer and design new effective and interpretable model architectures.

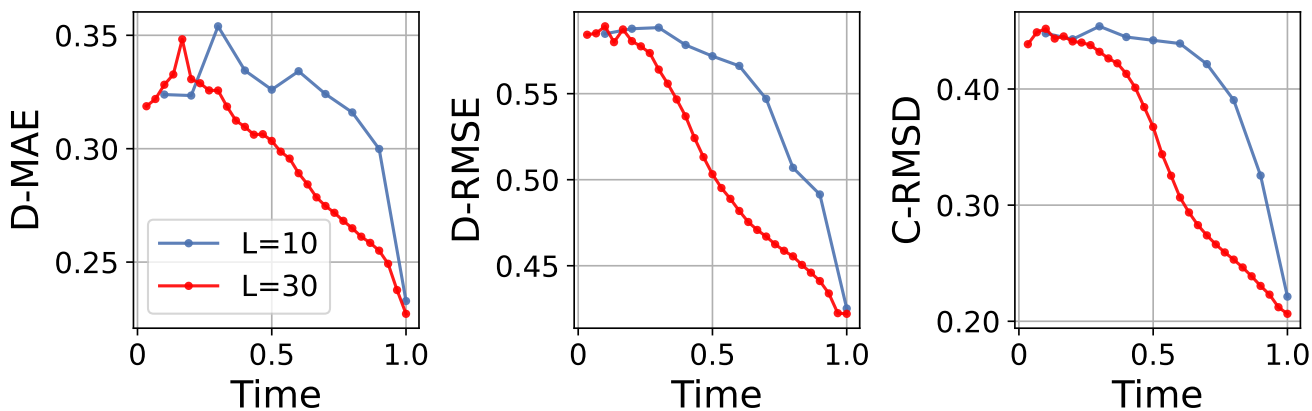


Figure 5: The comparison for WGFormer₁₀ and WGFormer₃₀ on optimization processes from $t = 0$ to $t = 1$. For each model and $l = 1, \dots, L$, the point at $t = \frac{l}{L}$ corresponds to the performance achieved by l layers.

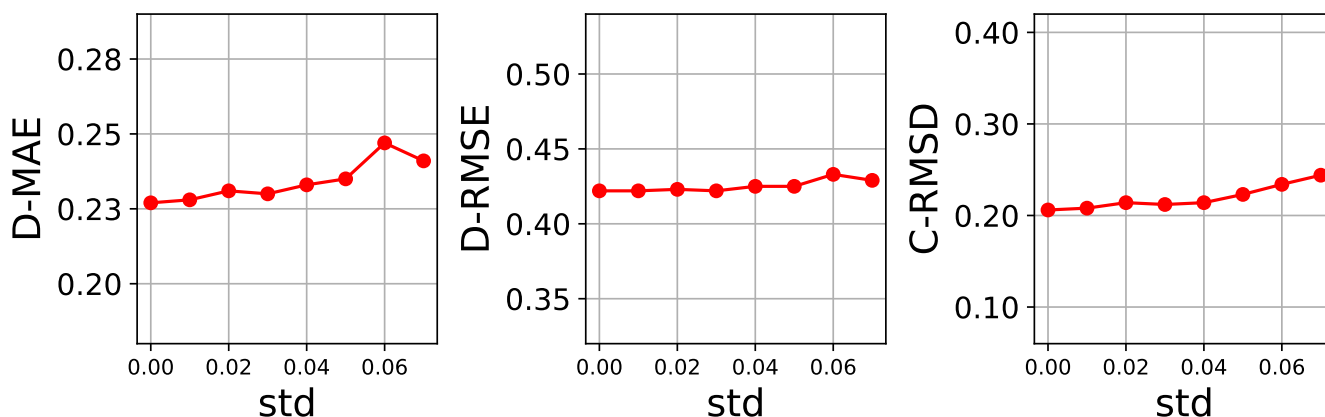


Figure 6: The robustness test of our model to data noise.

References

- [1] G. Xu, Y. Jiang, P. Lei, Y. Yang, and J. Chen, “Gtmgc: Using graph transformer to predict molecule’s ground-state conformation,” in *The Twelfth International Conference on Learning Representations*, 2023.
- [2] A. Chatterjee, R. Walters, Z. Shafi, O. S. Ahmed, M. Sebek, D. Gysi, R. Yu, T. Eliassi-Rad, A.-L. Barabási, and G. Menichetti, “Improving the generalizability of protein-ligand binding predictions with ai-bind,” *Nature communications*, vol. 14, no. 1, p. 1989, 2023.
- [3] J. M. Paggi, A. Pandit, and R. O. Dror, “The art and science of molecular docking,” *Annual Review of Biochemistry*, vol. 93, 2024.
- [4] K. Moon, H.-J. Im, and S. Kwon, “3d graph contrastive learning for molecular property prediction,” *Bioinformatics*, vol. 39, no. 6, p. btad371, 2023.
- [5] M. Liu, C. Li, R. Chen, D. Cao, and X. Zeng, “Geometric deep learning for drug discovery,” *Expert Systems with Applications*, vol. 240, p. 122498, 2024.
- [6] O. M. Salo-Ahen, I. Alanko, R. Bhadane, A. M. Bonvin, R. V. Honorato, S. Hossain, A. H. Juffer, A. Kabadev, M. Lahtela-Kakkonen, A. S. Larsen *et al.*, “Molecular dynamics simulations in drug discovery and pharmaceutical development,” *Processes*, vol. 9, no. 1, p. 71, 2020.

- [7] P. Pracht, F. Bohle, and S. Grimme, “Automated exploration of the low-energy chemical space with fast quantum chemical methods,” *Physical Chemistry Chemical Physics*, vol. 22, no. 14, pp. 7169–7192, 2020.
- [8] D. S. Sholl and J. A. Steckel, *Density functional theory: a practical introduction*. John Wiley & Sons, 2022.
- [9] S. Axelrod and R. Gomez-Bombarelli, “Geom, energy-annotated molecular conformations for property prediction and molecular generation,” *Scientific Data*, vol. 9, no. 1, p. 185, 2022.
- [10] G. Landrum *et al.*, “Rdkit: A software suite for cheminformatics, computational chemistry, and predictive modeling,” *Greg Landrum*, vol. 8, no. 31.10, p. 5281, 2013.
- [11] H. Wang, T. Fu, Y. Du, W. Gao, K. Huang, Z. Liu, P. Chandak, S. Liu, P. Van Katwyk, A. Deac *et al.*, “Scientific discovery in the age of artificial intelligence,” *Nature*, vol. 620, no. 7972, pp. 47–60, 2023.
- [12] J. Abramson, J. Adler, J. Dunger, R. Evans, T. Green, A. Pritzel, O. Ronneberger, L. Willmore, A. J. Ballard, J. Bambrick *et al.*, “Accurate structure prediction of biomolecular interactions with alphafold 3,” *Nature*, pp. 1–3, 2024.
- [13] M. Xu, W. Wang, S. Luo, C. Shi, Y. Bengio, R. Gomez-Bombarelli, and J. Tang, “An end-to-end framework for molecular conformation generation via bilevel programming,” in *International conference on machine learning*. PMLR, 2021, pp. 11 537–11 547.
- [14] Z. Xu, Y. Luo, X. Zhang, X. Xu, Y. Xie, M. Liu, K. Dickerson, C. Deng, M. Nakata, and S. Ji, “Molecule3d: A benchmark for predicting 3d geometries from molecular graphs,” *arXiv preprint arXiv:2110.01717*, 2021.
- [15] J. Guan, W. W. Qian, Q. Liu, W.-Y. Ma, J. Ma, and J. Peng, “Energy-inspired molecular conformation optimization,” in *International Conference on Learning Representations*, 2022.
- [16] G. Zhou, Z. Gao, Q. Ding, H. Zheng, H. Xu, Z. Wei, L. Zhang, and G. Ke, “Uni-mol: A universal 3d molecular representation learning framework,” in *The Eleventh International Conference on Learning Representations*, 2022.
- [17] S. Feng, Y. Ni, M. Li, Y. Huang, Z.-M. Ma, W.-Y. Ma, and Y. Lan, “Unicorn: A unified contrastive learning approach for multi-view molecular representation learning,” in *Forty-first International Conference on Machine Learning*, 2024.
- [18] F. Fuchs, D. Worrall, V. Fischer, and M. Welling, “Se (3)-transformers: 3d roto-translation equivariant attention networks,” *Advances in neural information processing systems*, vol. 33, pp. 1970–1981, 2020.
- [19] V. G. Satorras, E. Hoogeboom, and M. Welling, “E (n) equivariant graph neural networks,” in *International conference on machine learning*. PMLR, 2021, pp. 9323–9332.
- [20] M. E. Sander, P. Ablin, M. Blondel, and G. Peyré, “Sinkformers: Transformers with doubly stochastic attention,” in *International Conference on Artificial Intelligence and Statistics*. PMLR, 2022, pp. 3515–3530.
- [21] M. Cuturi, “Sinkhorn distances: Lightspeed computation of optimal transport,” *Advances in neural information processing systems*, vol. 26, 2013.
- [22] F. Santambrogio, “{Euclidean, metric, and Wasserstein} gradient flows: an overview,” *Bulletin of Mathematical Sciences*, vol. 7, pp. 87–154, 2017.
- [23] E. Mansimov, O. Mahmood, S. Kang, and K. Cho, “Molecular geometry prediction using a deep generative graph neural network,” *Scientific reports*, vol. 9, no. 1, p. 20381, 2019.

- [24] D. P. Kingma and M. Welling, “Auto-encoding variational bayes,” *arXiv preprint arXiv:1312.6114*, 2013.
- [25] M. Xu, S. Luo, Y. Bengio, J. Peng, and J. Tang, “Learning neural generative dynamics for molecular conformation generation,” *arXiv preprint arXiv:2102.10240*, 2021.
- [26] C. Shi, S. Luo, M. Xu, and J. Tang, “Learning gradient fields for molecular conformation generation,” in *International conference on machine learning*. PMLR, 2021, pp. 9558–9568.
- [27] I. Kobyzev, S. J. Prince, and M. A. Brubaker, “Normalizing flows: An introduction and review of current methods,” *IEEE transactions on pattern analysis and machine intelligence*, vol. 43, no. 11, pp. 3964–3979, 2020.
- [28] Y. Song, J. Sohl-Dickstein, D. P. Kingma, A. Kumar, S. Ermon, and B. Poole, “Score-based generative modeling through stochastic differential equations,” in *International Conference on Learning Representations*, 2020.
- [29] M. Xu, L. Yu, Y. Song, C. Shi, S. Ermon, and J. Tang, “Geodiff: A geometric diffusion model for molecular conformation generation,” in *International Conference on Learning Representations*, 2021.
- [30] B. Jing, G. Corso, J. Chang, R. Barzilay, and T. Jaakkola, “Torsional diffusion for molecular conformer generation,” *Advances in Neural Information Processing Systems*, vol. 35, pp. 24 240–24 253, 2022.
- [31] J. Ho, A. Jain, and P. Abbeel, “Denoising diffusion probabilistic models,” *Advances in neural information processing systems*, vol. 33, pp. 6840–6851, 2020.
- [32] C. Ying, T. Cai, S. Luo, S. Zheng, G. Ke, D. He, Y. Shen, and T.-Y. Liu, “Do transformers really perform badly for graph representation?” *Advances in neural information processing systems*, vol. 34, pp. 28 877–28 888, 2021.
- [33] T. Kim, H. Seo, S. Ahn, and E. Yang, “Rebind: Enhancing ground-state molecular conformation via force-based graph rewiring,” *arXiv preprint arXiv:2410.14696*, 2024.
- [34] A. Tsy-pin, L. A. Ugadiarov, K. Khrabrov, A. Telepov, E. Rumiantsev, A. Skrynnik, A. Panov, D. P. Vetrov, E. Tutubalina, and A. Kadurin, “Gradual optimization learning for conformational energy minimization,” in *The Twelfth International Conference on Learning Representations*, 2024.
- [35] E. Weinan, J. Han, and Q. Li, “A mean-field optimal control formulation of deep learning,” *Research in the Mathematical Sciences*, vol. 1, no. 6, pp. 1–41, 2018.
- [36] S. Dutta, T. Gautam, S. Chakrabarti, and T. Chakraborty, “Redesigning the transformer architecture with insights from multi-particle dynamical systems,” *Advances in Neural Information Processing Systems*, vol. 34, pp. 5531–5544, 2021.
- [37] X. Wang, H. Zhao, W.-w. Tu, and Q. Yao, “Automated 3d pre-training for molecular property prediction,” in *Proceedings of the 29th ACM SIGKDD Conference on Knowledge Discovery and Data Mining*, 2023, pp. 2419–2430.
- [38] S. Riniker and G. A. Landrum, “Better informed distance geometry: using what we know to improve conformation generation,” *Journal of chemical information and modeling*, vol. 55, no. 12, pp. 2562–2574, 2015.
- [39] B. Scholkopf, K.-K. Sung, C. J. Burges, F. Girosi, P. Niyogi, T. Poggio, and V. Vapnik, “Comparing support vector machines with gaussian kernels to radial basis function classifiers,” *IEEE transactions on Signal Processing*, vol. 45, no. 11, pp. 2758–2765, 1997.

- [40] H. Kim, G. Papamakarios, and A. Mnih, “The lipschitz constant of self-attention,” in *International Conference on Machine Learning*. PMLR, 2021, pp. 5562–5571.
- [41] A. Vaswani, N. Shazeer, N. Parmar, J. Uszkoreit, L. Jones, A. N. Gomez, Ł. Kaiser, and I. Polosukhin, “Attention is all you need,” *Advances in neural information processing systems*, vol. 30, 2017.
- [42] K. He, X. Zhang, S. Ren, and J. Sun, “Deep residual learning for image recognition,” in *Proceedings of the IEEE conference on computer vision and pattern recognition*, 2016, pp. 770–778.
- [43] W. Weinan, “A proposal on machine learning via dynamical systems,” *Communications in Mathematics and Statistics*, vol. 5, no. 1, pp. 1–11, 2017.
- [44] M. Renardy and R. C. Rogers, *An introduction to partial differential equations*. Springer Science & Business Media, 2006, vol. 13.
- [45] R. Jordan, D. Kinderlehrer, and F. Otto, “The variational formulation of the fokker–planck equation,” *SIAM journal on mathematical analysis*, vol. 29, no. 1, pp. 1–17, 1998.
- [46] G. Peyré, M. Cuturi *et al.*, “Computational optimal transport: With applications to data science,” *Foundations and Trends[®] in Machine Learning*, vol. 11, no. 5-6, pp. 355–607, 2019.
- [47] C. Wang and S. Mahadevan, “Manifold alignment using procrustes analysis,” in *Proceedings of the 25th international conference on Machine learning*, 2008, pp. 1120–1127.
- [48] R. Ramakrishnan, P. O. Dral, M. Rupp, and O. A. Von Lilienfeld, “Quantum chemistry structures and properties of 134 kilo molecules,” *Scientific data*, vol. 1, no. 1, pp. 1–7, 2014.
- [49] Y.-L. Liao and T. Smidt, “Equiformer: Equivariant graph attention transformer for 3d atomistic graphs,” in *International Conference on Learning Representations*, 2023.
- [50] W. Hu, B. Liu, J. Gomes, M. Zitnik, P. Liang, V. Pande, and J. Leskovec, “Strategies for pre-training graph neural networks,” in *International Conference on Learning Representations*, 2020.
- [51] S. Brody, U. Alon, and E. Yahav, “How attentive are graph attention networks?” in *International Conference on Learning Representations*, 2021.
- [52] L. Rampášek, M. Galkin, V. P. Dwivedi, A. T. Luu, G. Wolf, and D. Beaini, “Recipe for a general, powerful, scalable graph transformer,” *Advances in Neural Information Processing Systems*, vol. 35, pp. 14 501–14 515, 2022.

A SE(3)-Equivariance

To prove that our whole auto-encoding framework is SE(3)-equivariant, we will verify that if the input low-quality conformation $\tilde{\mathcal{C}} = [\tilde{\mathbf{c}}_i] \in \mathbb{R}^{N \times 3}$ undergo an SE(3)-transformation (\mathbf{Q}, \mathbf{t}) , where $\mathbf{Q} \in \mathbb{R}^{3 \times 3}$ is a rotation matrix and $\mathbf{t} \in \mathbb{R}^3$ is a translation, the predicted ground-state conformation $\hat{\mathcal{C}} = [\hat{\mathbf{c}}_i] \in \mathbb{R}^{N \times 3}$ will transform in the same manner. Specifically, let $\tilde{\mathcal{C}}' = [\tilde{\mathbf{c}}'_i] = [\mathbf{Q}\tilde{\mathbf{c}}_i + \mathbf{t}]$, we aim to demonstrate that the corresponding output satisfies $\hat{\mathcal{C}}' = [\hat{\mathbf{c}}'_i] = [\mathbf{Q}\hat{\mathbf{c}}_i + \mathbf{t}]$.

In the **encoding phase**, the initial atom-level representation $\mathbf{X}^{(0)} = [\mathbf{x}_i^{(0)}] \in \mathbb{R}^{N \times D}$ can be extracted as follows:

$$\mathbf{x}_i^{(0)} = f(v_i), \quad (22)$$

where f is an embedding function dependent only on atom type v_i . Since atom type is independent of the geometric coordinates, the initial atom-level representation $\mathbf{X}^{(0)} = [\mathbf{x}_i^{(0)}]$ remains unchanged under the SE(3)-transformation.

Meanwhile, the initial interatomic relational representation $\mathbf{R}^{(0)} = [\mathbf{r}_{ij}^{(0)}] \in \mathbb{R}^{N \times N \times H}$ can be extracted as follows:

$$\mathbf{r}_{ij}^{(0)} = \mathcal{N}(\tilde{d}_{ij} \mathbf{u}_{v_i v_j} + \mathbf{v}_{v_i v_j}; \boldsymbol{\mu}, \boldsymbol{\sigma}), \quad (23)$$

where $\tilde{d}_{ij} = \|\tilde{\mathbf{c}}_i - \tilde{\mathbf{c}}_j\|_2$ is the interatomic distance, which remains unchanged under the SE(3)-transformation (\mathbf{Q}, \mathbf{t}) , i.e.,

$$\tilde{d}'_{ij} = \|\tilde{\mathbf{c}}'_i - \tilde{\mathbf{c}}'_j\|_2 = \|(\mathbf{Q}\tilde{\mathbf{c}}_i + \mathbf{t}) - (\mathbf{Q}\tilde{\mathbf{c}}_j + \mathbf{t})\|_2 = \|\mathbf{Q}\tilde{\mathbf{c}}_i - \mathbf{Q}\tilde{\mathbf{c}}_j\|_2 = \|\tilde{\mathbf{c}}_i - \tilde{\mathbf{c}}_j\|_2 = \tilde{d}_{ij}, \quad (24)$$

The initial interatomic relational representation $\mathbf{R}^{(0)} = [\mathbf{r}_{ij}^{(0)}]$ also remains unchanged under the SE(3)-transformation.

Furthermore, since the initial atom-level representation $\mathbf{X}^{(0)} = [\mathbf{x}_i^{(0)}]$ and interatomic relational representation $\mathbf{R}^{(0)} = [\mathbf{r}_{ij}^{(0)}]$ remains unchanged under the SE(3)-transformation, the final atom-level representation $\mathbf{X}^{(L)} = [\mathbf{x}_i^{(L)}]$ and interatomic relational representation $\mathbf{R}^{(L)} = [\mathbf{r}_{ij}^{(L)}]$ will also remain unchanged under the SE(3)-transformation. In other words, $\mathbf{X}^{(0)} = [\mathbf{x}_i^{(0)}]$, $\mathbf{R}^{(0)} = [\mathbf{r}_{ij}^{(0)}]$, $\mathbf{X}^{(L)} = [\mathbf{x}_i^{(L)}]$ and $\mathbf{R}^{(L)} = [\mathbf{r}_{ij}^{(L)}]$ are all SE(3)-invariant.

In the **decoding phase**, the predicted ground-state conformation $\hat{\mathcal{C}} = [\hat{\mathbf{c}}_i]$ can be computed as follows:

$$\hat{\mathbf{c}}_i = \tilde{\mathbf{c}}_i + \sum_{j=1}^N \frac{\text{MLP}(\mathbf{r}_{ij}^{(L)} - \mathbf{r}_{ij}^{(0)})(\tilde{\mathbf{c}}_i - \tilde{\mathbf{c}}_j)}{N}, \quad (25)$$

Under the SE(3)-transformation (\mathbf{Q}, \mathbf{t}) , the input coordinates $\tilde{\mathbf{c}}'_i$ and $\tilde{\mathbf{c}}'_j$ are transformed as:

$$\tilde{\mathbf{c}}'_i = \mathbf{Q}\tilde{\mathbf{c}}_i + \mathbf{t}, \quad \tilde{\mathbf{c}}'_j = \mathbf{Q}\tilde{\mathbf{c}}_j + \mathbf{t}, \quad (26)$$

The relative displacements in the decoding equation are then given by:

$$\tilde{\mathbf{c}}'_i - \tilde{\mathbf{c}}'_j = (\mathbf{Q}\tilde{\mathbf{c}}_i + \mathbf{t}) - (\mathbf{Q}\tilde{\mathbf{c}}_j + \mathbf{t}) = \mathbf{Q}(\tilde{\mathbf{c}}_i - \tilde{\mathbf{c}}_j), \quad (27)$$

As the MLP operates on SE(3)-invariant inputs $(\mathbf{r}_{ij}^{(L)} - \mathbf{r}_{ij}^{(0)})$, the updated predicted coordinates become:

$$\hat{\mathbf{c}}'_i = \tilde{\mathbf{c}}'_i + \sum_{j=1}^N \frac{\text{MLP}(\mathbf{r}_{ij}^{(L)} - \mathbf{r}_{ij}^{(0)})(\tilde{\mathbf{c}}'_i - \tilde{\mathbf{c}}'_j)}{N}, \quad (28)$$

Expanding $\tilde{\mathbf{c}}'_i$ and $\tilde{\mathbf{c}}'_j$ in terms of \mathbf{Q} and \mathbf{t} , we have:

$$\hat{\mathbf{c}}'_i = (\mathbf{Q}\tilde{\mathbf{c}}_i + \mathbf{t}) + \sum_{j=1}^N \frac{\text{MLP}(\mathbf{r}_{ij}^{(L)} - \mathbf{r}_{ij}^{(0)})\mathbf{Q}(\tilde{\mathbf{c}}'_i - \tilde{\mathbf{c}}'_j)}{N}, \quad (29)$$

Since the rotation matrix \mathbf{Q} is a linear transformation, it factors out from the weighted sum:

$$\hat{\mathbf{c}}'_i = \mathbf{Q} \left(\tilde{\mathbf{c}}_i + \sum_{j=1}^N \frac{\text{MLP}(\mathbf{r}_{ij}^{(L)} - \mathbf{r}_{ij}^{(0)})(\tilde{\mathbf{c}}_i - \tilde{\mathbf{c}}_j)}{N} \right) + \mathbf{t}, \quad (30)$$

The term in parentheses is simply the original $\hat{\mathbf{c}}_i$, i.e.,

$$\hat{\mathbf{c}}'_i = \mathbf{Q}\hat{\mathbf{c}}_i + \mathbf{t}, \quad (31)$$

Therefore, our whole auto-encoding framework is SE(3)-equivariant.

B Proofs of Key Theoretical Results

In principle, the proofs of our theoretical results are based on the same techniques used in [20]. However, because of considering the interatomic relations and their updates, WGFormer corresponds to Wasserstein gradient flows in a more strict condition and the energy function it minimized considers the relational information of molecular conformation.

B.1 Proof of Proposition 4.1

Proof. Recall that $\mu = \sum_{i=1}^N \mu_i$, $\mu_i \in \mathcal{M}(\mathbb{R}^D)$ for $i = 1, \dots, N$. In addition, we impose the standard sufficient regularity assumption on each μ_i . When each component measure is a Dirac measure, i.e., $\mu_i = \delta_{\mathbf{x}_i}$, we have $\mu = \sum_{i=1}^N \delta_{\mathbf{x}_i}$. In such a situation, we rewrite the energy function in Eq. 15 as

$$E^0(\mu) = \frac{1}{2} \iint_{\mathbb{R}^D \times \mathbb{R}^D} \underbrace{\exp(\mathbf{x}^\top \mathbf{A} \mathbf{x}' + r(\mathbf{x}, \mathbf{x}'))}_{k^0(\mathbf{x}, \mathbf{x}')} d\mu(\mathbf{x}) d\mu(\mathbf{x}') = \frac{1}{2} \sum_{i,j=1}^N \exp(\mathbf{x}_i^\top \mathbf{A} \mathbf{x}_j + r_{ij}). \quad (32)$$

Accordingly, its first variation at μ is

$$\frac{\delta E^0}{\delta \mu}(\mu)(\mathbf{x}) = \int_{\mathbb{R}^D} \exp(\mathbf{x}^\top \mathbf{A} \mathbf{x}' + r(\mathbf{x}, \mathbf{x}')) d\mu(\mathbf{x}') = \sum_{j=1}^N \exp(\mathbf{x}^\top \mathbf{A} \mathbf{x}_j + r(\mathbf{x}, \mathbf{x}_j)). \quad (33)$$

In this case, the operator $T_\mu^0(\mathbf{x})$ becomes

$$T_\mu^0(\mathbf{x}) = - \int_{\mathbb{R}^D} \exp(\mathbf{x}^\top \mathbf{A} \mathbf{x}' + r(\mathbf{x}, \mathbf{x}')) \mathbf{A} \mathbf{x}' d\mu(\mathbf{x}') = - \sum_{j=1}^N \exp(\mathbf{x}^\top \mathbf{A} \mathbf{x}_j + r(\mathbf{x}, \mathbf{x}_j)) \mathbf{A} \mathbf{x}_j. \quad (34)$$

Then, we have

$$\nabla_W E^0(\mu)(\mathbf{x}) = \sum_{j=1}^N \nabla_{\mathbf{x}} \exp(\mathbf{x}^\top \mathbf{A} \mathbf{x}_j + r(\mathbf{x}, \mathbf{x}_j)) = \sum_{j=1}^N \exp(\mathbf{x}^\top \mathbf{A} \mathbf{x}_j + r(\mathbf{x}, \mathbf{x}_j)) \mathbf{A} \mathbf{x}_j = -T_\mu^0(\mathbf{x}). \quad (35)$$

In general, given $\mu = \sum_{i=1}^N \mu_i$, we define an energy function of $\{\mu_i\}_{i=1}^N$ with $M \rightarrow \infty$ as

$$\begin{aligned} E^\infty(\{\mu_i\}_{i=1}^N) &= \frac{1}{2} \inf_{\pi \in \Pi(\mu, \mu)} \sum_{i,j=1}^N \iint_{\mathbb{R}^D \times \mathbb{R}^D} \pi(\mathbf{x}, \mathbf{x}') (\mathbf{x}^\top \mathbf{A} \mathbf{x}' + r_{ij}) + \pi(\mathbf{x}, \mathbf{x}') \log \pi(\mathbf{x}, \mathbf{x}') d\mu_i(\mathbf{x}) d\mu_j(\mathbf{x}') \\ &= \frac{1}{2} \inf_{\pi \in \Pi(\mu, \mu)} \sum_{i,j=1}^N \iint_{\mathbb{R}^D \times \mathbb{R}^D} \pi(\mathbf{x}, \mathbf{x}') (\mathbf{x}^\top \mathbf{A} \mathbf{x}' + r_{ij}) d\mu_i(\mathbf{x}) d\mu_j(\mathbf{x}') - H(\pi), \end{aligned} \quad (36)$$

where $H(\pi) = -\iint_{\mathbb{R}^D \times \mathbb{R}^D} \pi(\mathbf{x}, \mathbf{x}') d\mu(\mathbf{x}) d\mu(\mathbf{x}')$ is the entropy of the coupling π . Essentially, Eq. 36 corresponds to an entropic optimal transport (EOT) problem defined for the mixture model μ .

Furthermore, when $\mu = \sum_{i=1}^N \delta_{\mathbf{x}_i}$, we can equivalently rewrite it as a function of μ and in a classic EOT format, i.e.,

$$\begin{aligned} E^\infty(\mu) &= \frac{1}{2} \min_{\pi \in \Pi(\mu, \mu)} \iint_{\mathbb{R}^D \times \mathbb{R}^D} \underbrace{(\mathbf{x}^\top \mathbf{A} \mathbf{x}' + r(\mathbf{x}, \mathbf{x}'))}_{\text{cost: } \log k^0(\mathbf{x}, \mathbf{x}')} \pi(\mathbf{x}, \mathbf{x}') d\mu(\mathbf{x}) d\mu(\mathbf{x}') - H(\pi) \\ &= \frac{1}{2} \int k^\infty(\mathbf{x}, \mathbf{x}') \log \frac{k^0(\mathbf{x}, \mathbf{x}')}{k^\infty(\mathbf{x}, \mathbf{x}')} d\mu(\mathbf{x}) d\mu(\mathbf{x}') \\ &= \frac{1}{2} \max_{f \in \mathcal{C}(\mathbb{R}^D)} \int f(\mathbf{x}) + f^c(\mathbf{x}) d\mu(\mathbf{x}). \end{aligned} \quad (37)$$

Here, the second equality in Eq. 37 means applying the Sinkhorn-scaling algorithm to solve the EOT problem (with $M \rightarrow \infty$), where k^∞ is the optimal coupling. The third equality in Eq. 37 is based on the duality of the EOT problem [46] and f^c is the soft c-transform defined as

$$f^c(\mathbf{x}') = -\log \left(\int_{\mathbb{R}^D} \exp(\log k^0(\mathbf{x}, \mathbf{x}') + f(\mathbf{x})) d\mu(\mathbf{x}) \right). \quad (38)$$

In such a situation, we can follow the proof in [20]: It has been known that when f is optimized, we have $f = f^c$, and $k^\infty(\mathbf{x}, \mathbf{x}') = \exp(\log k^0(\mathbf{x}, \mathbf{x}') + f(\mathbf{x}) + f(\mathbf{x}'))$. As a result, we have

$$\begin{aligned} \nabla_W E^\infty(\mu)(\mathbf{x}) &= \nabla_{\mathbf{x}} f(\mathbf{x}) \\ &= \int_{\mathbb{R}^D} \exp(f(\mathbf{x}) + f(\mathbf{x}') + \log k^0(\mathbf{x}, \mathbf{x}')) \nabla_{\mathbf{x}} \log k^0(\mathbf{x}, \mathbf{x}') d\mu(\mathbf{x}') \\ &= \int_{\mathbb{R}^D} k^\infty(\mathbf{x}, \mathbf{x}') \nabla_{\mathbf{x}} \log k^0(\mathbf{x}, \mathbf{x}') d\mu(\mathbf{x}') \\ &= \int_{\mathbb{R}^D} k^\infty(\mathbf{x}, \mathbf{x}) \mathbf{A} \mathbf{x}' d\mu(\mathbf{x}') \\ &= -T_\mu^\infty(\mathbf{x}). \end{aligned} \quad (39)$$

□

B.2 Proof of Proposition 4.2

Proof. Given non-Dirac measures $\{\mu_i\}_{i=1}^N$, we can fix each component measure except μ_i and minimize the energy function in Eq. 19, i.e., $\min_{\mu_i} E(\mu_i; \{\mu_j\}_{j \neq i})$. According to the work in [22], the first variation of $E(\mu_i; \{\mu_j\}_{j \neq i})$ at μ_i is

$$\begin{aligned} \frac{\delta E}{\delta \mu_i}(\mu_i)(\mathbf{x}) &= \frac{1}{2} \int_{\mathcal{X}} \exp(\mathbf{x}^\top \mathbf{A} \mathbf{x}' + r_{ii}) + \exp(\mathbf{x}'^\top \mathbf{A} \mathbf{x} + r_{ii}) d\mu_i(\mathbf{x}') + \\ &\quad \frac{1}{2} \sum_{j \neq i} \int_{\mathcal{X}} \exp(\mathbf{x}^\top \mathbf{A} \mathbf{x}' + r_{ij}) + \exp(\mathbf{x}'^\top \mathbf{A} \mathbf{x} + r_{ji}) d\mu_j(\mathbf{x}') \\ &= \sum_{j=1}^N \int_{\mathcal{X}} \exp(\mathbf{x}^\top \mathbf{A} \mathbf{x}' + r_{ij}) d\mu_j(\mathbf{x}'), \end{aligned} \quad (40)$$

where the second equality in Eq. 40 is because both \mathbf{A} and $\mathbf{R} = [r_{ij}]$ are symmetric matrices. By differentiation under the integral, we have

$$\begin{aligned}
 \nabla_W E(\mu_i; \{\mu_j\}_{j \neq i})(\mathbf{x}) &= \nabla \left(\frac{\delta E}{\delta \mu_i}(\mu_i) \right)(\mathbf{x}) \\
 &= \sum_{j=1}^N \int_{\mathcal{X}} \nabla_{\mathbf{x}} \exp(\mathbf{x}^\top \mathbf{A} \mathbf{x}' + r_{ij}) d\mu(\mathbf{x}') \\
 &= \sum_{j=1}^N \int_{\mathcal{X}} \exp(\mathbf{x}^\top \mathbf{A} \mathbf{x}' + r_{ij}) \mathbf{A} \mathbf{x}' d\mu(\mathbf{x}') \\
 &= -T_{\mu_i}^0(\mathbf{x}).
 \end{aligned}
 \tag{41}$$

□

C Implementation Details

C.1 Datasets

As mentioned in the main body, we also employ the widely used Molecule3D and QM9 datasets in our work in line with previous works, thus validating the effectiveness of our method:

- **Molecule3D.** The first benchmark introduced by [14] for the molecular ground-state conformation prediction task. It comprises approximately 4 million molecules, each with corresponding ground-state conformation determined through density functional theory (DFT) calculations. Additionally, it provides two dataset-splitting results (i.e., random-splitting and scaffold-splitting) to ensure a comprehensive evaluation.
- **QM9.** A small-scale quantum chemistry dataset proposed in [48], and the work in [1] further applies it to the molecular ground-state conformation prediction task. It comprises approximately 130,000 molecules with 9 heavy atoms, each with corresponding ground-state conformation determined through density functional theory (DFT) calculations. Besides, it adopts the identical dataset-splitting strategy described in [49].

Table 4: Scale overview of Molecule3D and QM9 datasets

Dataset	Splitting	Training	Validation	Test
Molecule3D	random-splitting	2,339,745	779,918	779,915
	scaffold-splitting	2,339,724	779,929	779,928
QM9	default	108,831	9,900	10,697

Table 4 provides the scale overview of the Molecule3D and QM9 datasets, outlining their division into training, validation, and test sets. For the Molecule3D dataset, random-splitting and scaffold-splitting strategies are applied, resulting in about 2.3 million molecules for training and approximately 0.78 million for both validation and test sets. The QM9 dataset utilizes a default splitting strategy described in [49], consisting of 108,831 molecules in the training set, 9,900 in the validation set, and 10,697 in the test set.

In addition, Figure 7 visualizes the distribution of atom count (including hydrogen atom) across these datasets. It demonstrates that molecules in the Molecule3D dataset generally contain more atoms than those in the QM9 dataset, thereby increasing the difficulty of predicting their corresponding ground-state molecular conformations. This observation aligns with the actual performance results in Table 1, thus explaining the decreased performance of all methods on the Molecule3D dataset relative to the QM9 dataset.

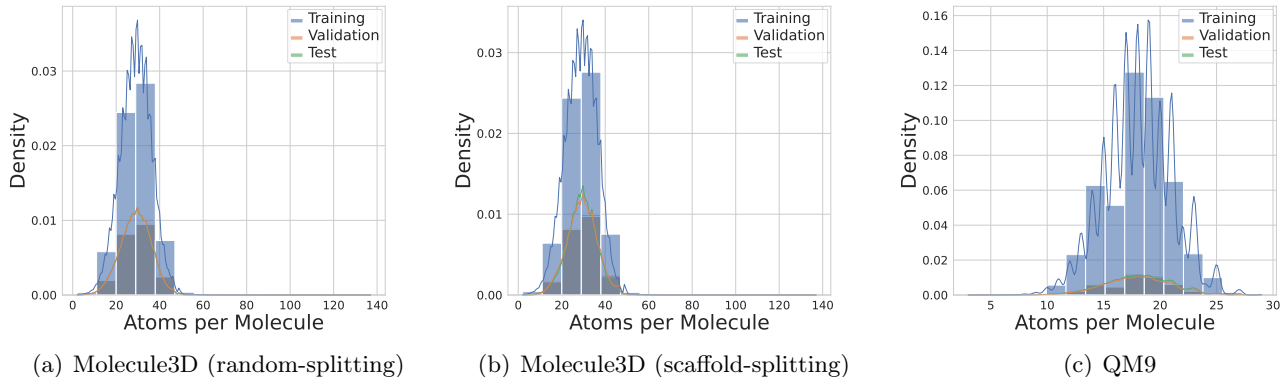


Figure 7: Atom count distribution of Molecule3D and QM9 datasets.

C.2 Baselines

As mentioned in the main body, we compare our method with 2D methods that predict ground-state conformations merely based on 2D molecular graphs and 3D methods that predict ground-state conformations from the conformation optimization perspective, to demonstrate the effectiveness of our method fully. The introductions of typical baselines are provided below:

- **GTMGC.** The typical 2D method proposed in [1], introduces a novel network based on Graph-Transformer (GT) to predict the molecular ground-state conformation from the corresponding 2D molecular graph in an end-to-end manner. In addition, it further designs various 2D baselines by replacing the backbone module with other models like **GINE** [50], **GATv2** [51], and **GPS** [52].
- **ConfOpt.** The typical 3D method proposed in [15], introduces variants of SE(3)-equivariant neural networks to predict the gradient field of the conformational energy landscape, and then optimize the input conformation by gradient descent. It can be divided into two variants: ConfOpt-TwoAtom, which considers only the relationships between atom pairs, and ConfOpt-ThreeAtom, which additionally accounts for the relationships among atom triplets. In addition, it further designs various 3D baselines by replacing the backbone module with other models like **SE(3)-Transformer** [18] and **EGNN** [19].

C.3 Evaluation Metrics

As mentioned in the main body, to guarantee a comprehensive and fair assessment, we also choose the same metrics introduced by [1], including mean-absolute-error of distances (D-MAE), root-mean-squared-error of distances (D-RMSE), and root-mean-square-deviation of coordinates (C-RMSD) to evaluate the performance.

Here, the specific definitions of these metrics can be expressed as follows:

$$\text{D-MAE}(\hat{\mathcal{D}}, \mathcal{D}^*) = \frac{1}{N^2} \sum_{i=1}^N \sum_{j=1}^N |\hat{d}_{ij} - d_{ij}^*|, \quad (42)$$

$$\text{D-RMSE}(\hat{\mathcal{D}}, \mathcal{D}^*) = \sqrt{\frac{1}{N^2} \sum_{i=1}^N \sum_{j=1}^N (\hat{d}_{ij} - d_{ij}^*)^2}, \quad (43)$$

$$\text{C-RMSD}(\hat{\mathcal{C}}, \mathcal{C}^*) = \sqrt{\frac{1}{N} \sum_{i=1}^N \|\hat{\mathbf{c}}_i - \mathbf{c}_i^*\|_2^2}. \quad (44)$$

where $\widehat{\mathcal{C}} = [\widehat{\mathbf{c}}_i] \in \mathbb{R}^{N \times 3}$ is the atom coordinates of predicted ground-state conformation, $\mathcal{C}^* = [\mathbf{c}_i^*] \in \mathbb{R}^{N \times 3}$ is the ground-truth aligned through Eq. 20, N is the number of atoms in the molecule, and $\widehat{d}_{ij} = \|\widehat{\mathbf{c}}_i - \widehat{\mathbf{c}}_j\|_2$, $d_{ij}^* = \|\mathbf{c}_i^* - \mathbf{c}_j^*\|_2$.

C.4 Hyperparameters

As mentioned in the main body, our model comprises 30 encoder layers (the number of WGFormer modules), each equipped with 64 attention heads. We train the whole model on the training set utilizing a single NVIDIA RTX 3090 GPU and select the optimal checkpoint based on performance evaluated on the corresponding validation set. The specific hyperparameters used across all datasets are summarized in Table 5.

Please note that the batch size on the Molecule3D dataset (i.e., 24 for random-splitting and 32 for scaffold-splitting) is purely decided by GPU memory limitation in our work.

Table 5: The specific hyperparameters on the Molecule3D and QM9 datasets

Hyperparameter	Molecule3D		QM9
	random-splitting	scaffold-splitting	
Batchsize	24	32	32
Learning Rate	5e-6	1e-5	2e-5
Auxiliary Loss Weight (λ)	0.125	0.125	0.125
Epoch	500	500	500
Adam Eps	1e-6	1e-6	1e-6
Adam Betas	(0.9, 0.99)	(0.9, 0.99)	(0.9, 0.99)
Num Encoder Layer (L)	30	30	30
Relational Representation Dimension (H)	64	64	64
Atom-level Representation Dimension (D)	512	512	512
Attention Head Dimension (D_a)	8	8	8

C.5 Hyperparameter Robustness

To provide a comprehensive analysis of our WGFormer’s performance, we have conducted more analysis studies on the QM9 dataset to demonstrate the hyperparameter robustness of our WGFormer.

As shown in Figure 8 and Figure 9, we evaluate the performance of our WGFormer under various hyperparameters, including different batch sizes and learning rates, on the QM9 dataset. The results consistently demonstrate that our WGFormer maintains stable and reliable performance under a wide range of hyperparameter configurations, especially for the batch size. This indicates the robustness of our WGFormer to these hyperparameters, ensuring practicality and adaptability in diverse training scenarios.

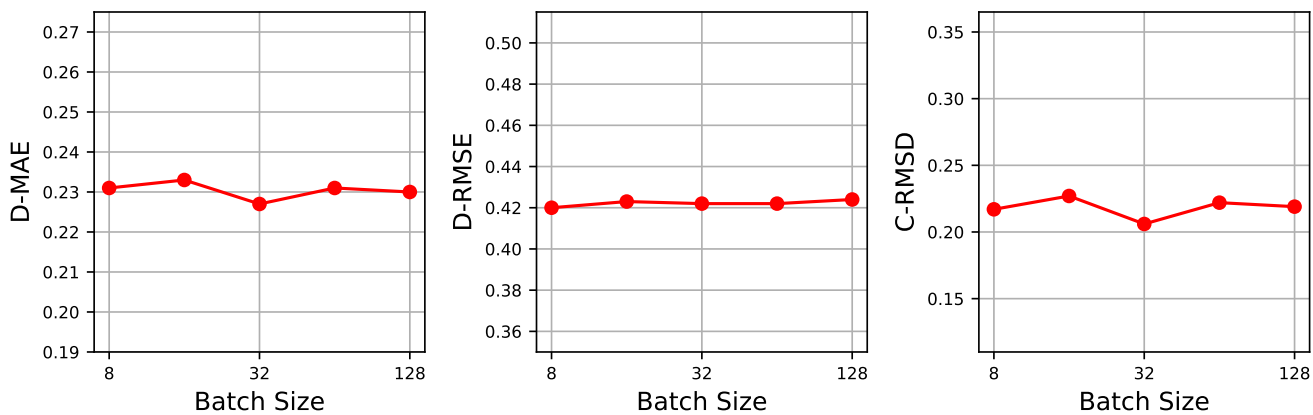


Figure 8: The performance of our WGFormer under different batch sizes on the QM9 dataset.

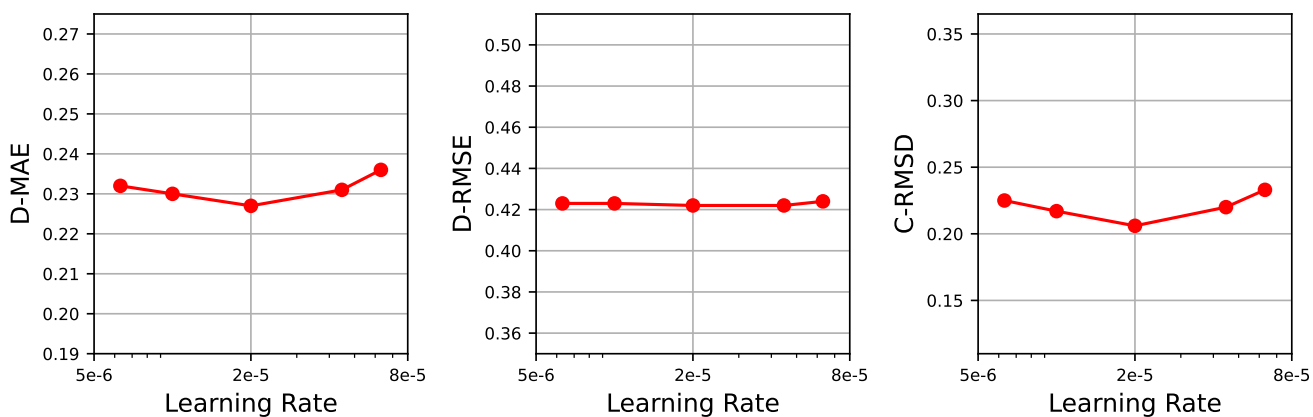


Figure 9: The performance of our WGFormer under different learning rates on the QM9 dataset.